Global transmission diagrams for evanescent waves in a nonlinear hyperbolic metamaterial

Munazza Zulfiqar Ali[1,*], Ashfaq Ahmad Bhatti[2], Qamar ul Haque[2], and Shahzad Mahmood[2]

[1]*Physics Department, Punjab University, Lahore 54590, Pakistan*
[2]*Theoretical Physics Division, PINSTECH, P.O. Nilore 44000, Islamabad, Pakistan*
**Corresponding author: munazzazulfiqar@yahoo.com*

Received April 2, 2015; accepted June 8, 2015; posted online July 23, 2015

A theoretical model of a nonlinear hyperbolic metamaterial is presented in the form of a stack of subwavelength layers of linear plasmonic and nonlinear dielectric materials. A broad picture of the properties of evanescent waves (high-k modes) in this stack is investigated by plotting global transmission diagrams. The presence of nonlinearity strongly modifies these diagrams. The emergence and modification of nonlinear evanescent waves is observed. Some signatures of nonlinear phenomenon such as formation of orbits and trajectories around fixed points are also seen in our work.

OCIS codes: 060.4370, 160.4670, 250.5403.
doi: 10.3788/COL201513.090601.

It has been strongly suggested that the future of photonics, plasmonics, and signal processing is related to the field of subwavelength optics[1–5]. Much theoretical and experimental research is being carried out to convert subwavelength evanescent waves into propagating modes[6–10]. One solution has come with the theoretical understanding and practical realization of hyperbolic metamaterials (HMMs). Metamaterials are artificially fabricated assemblies of subwavelength repeating units having unusual properties such as negative refraction, invisibility, super-lensing, and so on[11–17]. Metamaterials with hyperbolic dispersion is one of the most unusual classes of electromagnetic metamaterials. This hyperbolic dispersion originates from one of the principal components of the effective electric permittivity tensor of an anisotropic material having opposite sign to the other two principal components[18–21]. These HMMs can be practically realized in the form of a stack consisting of subwavelength alternate plasmonic and dielectric layers or a periodic arrangement of metallic nanowires in a dielectric host[22–27]. The greatest advantage of HMMs is the fact that they offer a multi-functional domain to realize novel electromagnetic devices at microwave, infrared, and optical frequencies. Due to the presence of hyperbolic dispersion it is possible to convert a portion of the evanescent waves into propagating waves even at optical frequencies. Such propagating modes have been termed high-k modes and their origin is coupled surface plasmon polaritons[28–32]. The characteristics of these coupled surface plasmon polaritons (sometimes called volume plasmon polaritons) have been studied extensively in linear HMMs. Optical effects can be strongly enhanced with nonlinear plasmonic metamaterials as highly localized fields are obtained in such structures. Certain recent studies have explored the potential of nonlinear HMMs. These include the nonlinear interaction of meta-atoms through optical coupling, intensity dependent transmission, all-optical modulation, the enhancement of the nonlinear optical response of metamaterials by using nonlocality, and so on[33–40]. In a very recent study, various phase-matching processes in nonlinear HMMs were systematically investigated[41].

In our work, we investigated the transmission characteristics of evanescent waves in a nonlinear HMM. We considered a stack consisting of subwavelength alternate linear plasmonic and nonlinear dielectric layers. The dielectric layers are assumed to exhibit Kerr-type third-order weak nonlinear coefficients. The nonlinearity is induced by the incident radiation at the frequencies of interest. The transmission characteristics are studied by plotting the global transmission diagrams. The terminology is borrowed from the work by Li *et al.*[42,43]. They studied the transmission characteristics of nonlinear photonic band gap structures for propagating waves by plotting density plots of the transmission coefficient in the intensity versus the wave vector plane. These are termed global transmission diagrams as a very broad picture of the transmission characteristics can be seen in such diagrams. They used the delta function approach for calculations by taking one of the layers to be very thin as compared to the other layer of the structure [42,43]. A discrete nonlinear map was obtained and they were able to identify different periodic behaviors and the existence of fractal-like structures in the transmission diagrams. Here we are using the transfer matrix approach[44,45] which is a more exact method as compared to the delta function approach. We have used two types of diagrams for nonlinear wave propagation. The density plots of $\log_{10} T$ (where T is transmission coefficient) are plotted in the wave vector versus intensity plane at a given frequency and the same plots are obtained in the frequency versus intensity plane for a given wave vector.

We model our theoretical work by considering a periodic stack consisting of alternate layers of a dispersive metal and a Kerr nonlinear dielectric material. The electric permittivity ε_m of the metal layer of width d_m is given by the Drude model, i.e., $\varepsilon_m = \varepsilon_\infty - \frac{\omega_p^2}{\omega^2 + i\gamma\omega}$, where ω_p and γ are the plasma frequency and the damping coefficient of the metal, respectively. For the dielectric layer of thickness d_d, the electric permittivity ε_d is taken to as $\varepsilon_d = \varepsilon_l + \alpha|E|^2$, where ε_l is the linear refractive index, α is the Kerr nonlinear coefficient, and $|E|^2$ is the intensity of the incident radiation. For our computational/numerical work, we have considered a Ag/TiO_2 structure with 20 alternate layers with a filling factor $f = 0.5$ (the filling factor of the structure is defined as $f = \frac{d_m}{d_m + d_d}$); values considered are

$$\varepsilon_\infty = 5, \quad \omega_p/2\pi = 2175 \text{ THz}, \quad \gamma/2\pi = 4.35 \text{ THz},$$
$$\varepsilon_l = 6.15, \quad d_d = d_m = 20 \text{ nm}, \quad \alpha = 9.4 \times 10^{-15} \text{ cm}^2 \text{ W}^{-1}. \tag{1}$$

Since the Kerr nonlinearity is a weak nonlinearity, the effective medium approximation (EMA), i.e., $k_{d,m} d_{d,m} \ll 1$, ($k_{d,m} = \varepsilon_{d,m} k_0$, k_0 is the free-space wave vector), still holds for the nonlinear structure. Using EMA, the periodic structure [Fig. 1(a)] can be represented by a uniaxial crystal (optical axis parallel to the z-axis in the present geometry) with a relative permittivity tensor defined as ($\varepsilon_{x,y} = \varepsilon_\perp$, $\varepsilon_z = \varepsilon_{||}$)

$$\bar{\bar{\varepsilon}} = \begin{pmatrix} \varepsilon_\perp & 0 & 0 \\ 0 & \varepsilon_\perp & 0 \\ 0 & 0 & \varepsilon_{||} \end{pmatrix}, \qquad \varepsilon_\perp = \frac{\varepsilon_d d_d + \varepsilon_m d_m}{d_d + d_m},$$
$$\varepsilon_{||} = \left[\frac{\varepsilon_d^{-1} d_d + \varepsilon_m^{-1} d_m}{d_d + d_m} \right]^{-1}. \tag{2}$$

The propagation of the transverse magnetic (TM) mode with the following dispersion relation under the conditions of EMA is considered

$$\frac{k_x^2 + k_y^2}{\varepsilon_{||}} + \frac{k_z^2}{\varepsilon_\perp} = \frac{\omega^2}{c^2}. \tag{3}$$

Equation (3) represents a hyperbola under the condition $\varepsilon_\perp \varepsilon_{||} < 0$. The validity of the EMA has been studied extensively in many recent studies[29,32] and an excellent agreement with exact calculations (based on the Bloch theorem) for small k values is observed, but it deviates somewhat for high-k values. Since here we are concerned with the high-k modes (the evanescent waves), instead of using the EMA, the transmission coefficient of the structure is computed by using the transfer matrix approach[44,45]. In this approach the tangential components of the electric and magnetic fields across a layer are related through the matrix equation

$$\begin{bmatrix} E \\ H \end{bmatrix}_z = \begin{bmatrix} \cos k_j d_j - \frac{\varepsilon_j}{k_j} \sin k_j d_j \\ \frac{k_j}{\varepsilon_j} \sin k_j d_j \cos k_j d_j \end{bmatrix} \begin{bmatrix} E \\ H \end{bmatrix}_{z+d_j}, \tag{4}$$

where $k_j = \sqrt{\varepsilon_j w - k_x^2}$.

For the nonlinear wave propagation, the permittivity essentially depends on the electric field intensity inside the layer that may vary significantly if the layer thickness is greater than the wavelength of the incident radiation. Here, the layer thickness is assumed to be subwavelength, so local fields are almost uniform inside the nonlinear layer and their average value is safely taken to compute the nonlinear permittivity of the dielectric layer.

For the computational work, the frequencies, wave vectors, and field intensities are used in dimensionless units, as follows

$$w = \frac{\omega d}{c}, \qquad \kappa = kd, \qquad I = \alpha|E|^2. \tag{5}$$

Initially we have plotted effective parameters for the linear case, i.e., taking α to be zero in Figs. 1(b) and 1(c). The Type II behavior ($\varepsilon_\perp < 0, \varepsilon_{||} > 0$) lies in the frequency $w < 0.8$ (dimensionless units) and the Type I ($\varepsilon_\perp > 0, \varepsilon_{||} < 0$) lies in the frequency region $w > 0.8$. For the filling factor of 0.5, there is no frequency gap between Type I and Type II HMMs. Dispersion curves in these regions are shown in Fig. 2. It is obvious that in a Type I metamaterial, only high-k modes exist whereas in a Type II metamaterial high as well as low k modes are present.

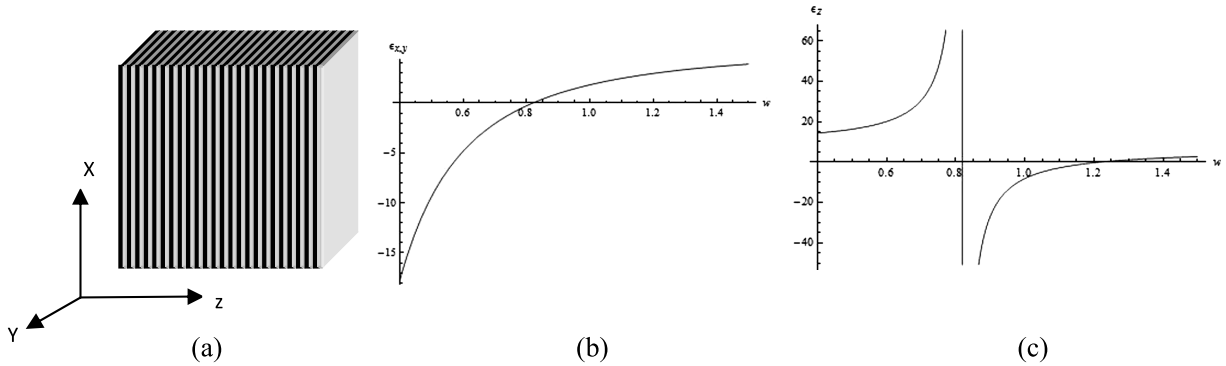

Fig. 1. (a) Schematic diagram; plots of (b) $\varepsilon_{x,y}$; and (c) ε_z versus w.

Figure 3 shows the linear case for a Type II HMM. It is a density plot of the tranmission coefficient in $\log_{10} T$ scale for the transverse wavevector $k = k_x/k_0$ versus frequency w. Here we have considered the evanescent waves, i.e., $k > 1$. The black regions correspond to infinitesimal small value of $\log_{10} T$ and indicate no transmission regions whereas the apprearance of white regions correspond to finite values of $\log_{10} T$ and indicate transmitting modes. In Fig. 3, the bright band corresponding to characteristc

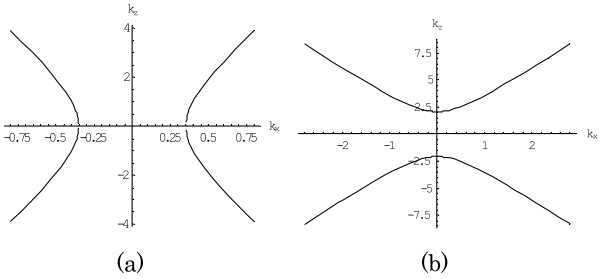

Fig. 2. (a) Plot of k_x versus k_z for a Type II HMM at $w = 0.1$; (b) same plot for a Type I HMM at $w = 1.2$.

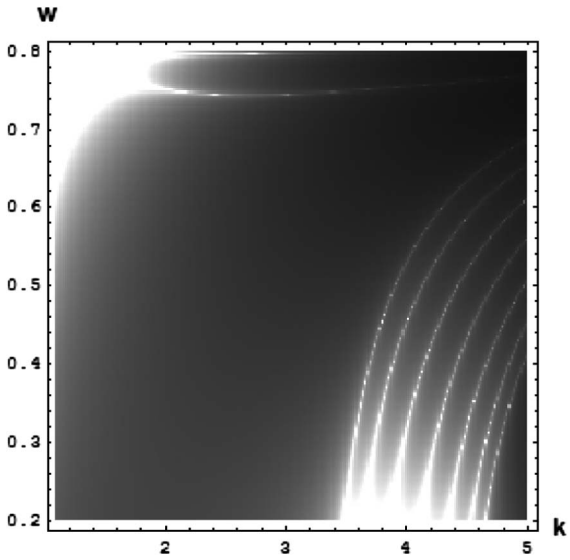

Fig. 3. Global transmission diagram of a Type II HMM.

surface plasmon polariton dispersion[23] and high-k transmission modes[29,32] can be clearly seen. The interesting thing is that most of Fig. 3 is black, indicating no transmission region for linear wave propagation.

Now we analyze different portions of the graphs for nonlinear wave propagations. Figure 4(a) is the isofrequency ($w = 0.6$) density plot of the transmission coefficient in $\log_{10} T$ scale for nonlinear wave propagation; the horizontal axis shows the transverse wave vector ($k > 1$, i.e., evanescent waves) whereas the verticle axis shows the dimensionless intensity of the incident wave.

It is obvious that the transmission properties are strongly modulated by the presence of nonlinearity. The appearance of transmission modes and formation of periodic patterns can be seen in the Figs. 4(a)–4(c). In Figs. 4(b) and 4(c) certain portions of Fig. 4(a) are shown in magnified scale. Figure 4(b) particularly shows the appearance of self-similar (fractal-like) paterns. It is also easy to identify the presence of an unstable fixed point (saddle) from where the nearby stable trajectories (white regions) are diverging hyperbolically. In Fig. 4(c) it is obvious that high-k modes are finely separated from one another on the intensity scale. Such a kind of fine separation can be used for modeling fine filters of evanescent waves. Here it shoud be noted that the emergence of new transmission features is a sole effect of nonlinearity induced by the incident radiation since the structure under consideration is investigated beyond the Fabry–Perot resonance condition[30,31] (i.e., the total length of the structure being integral multiple of half wavelengths inside the layers). If this condition holds, both linear and nonlinear transmission diagrams will be affected in the same manner.

Next in Figs. 5(a)–5(c) the density plots of the transmission coefficient in $\log_{10} T$ in the frequency versus intensity plane at a given wavevector ($k = 3$) for a Type II HMM are shown. The emergence of propagating modes (white regions) is again seen in these diagrames in the otherwise (linear) nonpropagating region. Each of Figs. 5(b) and 5(c) is blown up on the horizontal scale (frequency) as well as on the verticle scale (intensity) scale as compared to Fig. 5(a); again the formation of periodic and self-similiar structures within structures is obvious. The existence of

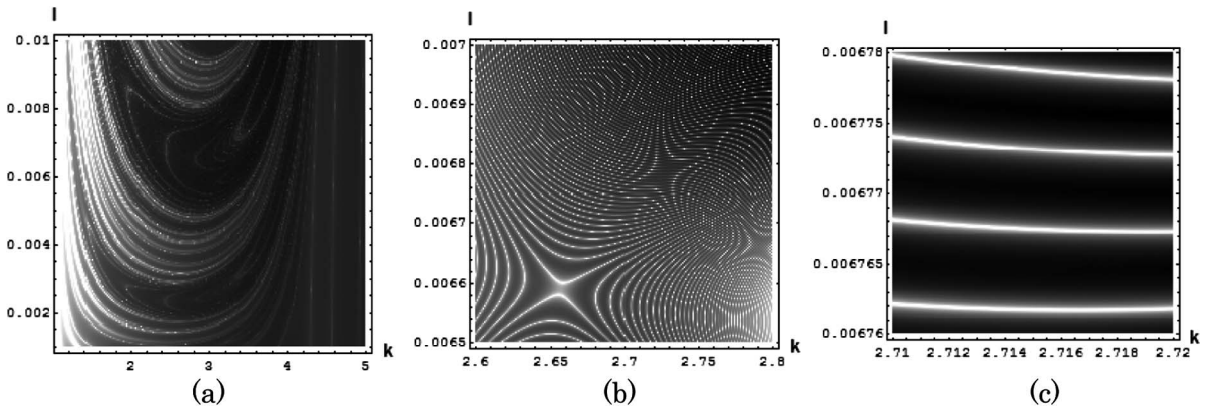

Fig. 4. (a) Global transmission diagram for k versus I at $w = 0.6$; (b) and (c) magnified portions of (a).

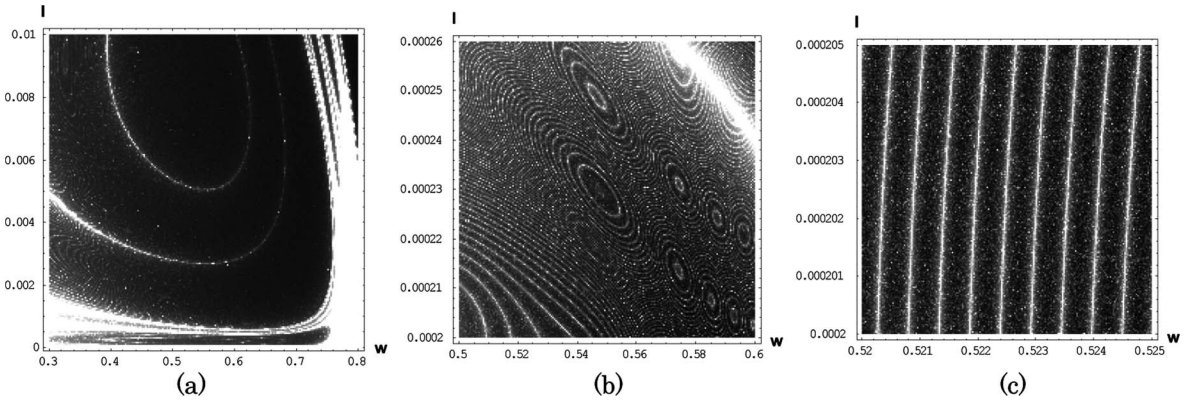

Fig. 5. (a) Global transmission diagram for w versus I at $k = 3$; (b) and (c) magnified portions of (a).

central (elliptic) type fixed points is obvious in Fig. 5. The stable trajecories (white regions) are orbitting round these fixed points in closed paths. Figure 5(c) shows fine separation of transmitting modes on the frequency axis; the phenomenon can be expoloited for fine tuning of frquencies for evanescent waves.

In the Type I HMM, two components of the permittivity tensor ($\varepsilon_x = \varepsilon_x = \varepsilon_\perp > 0$) are positive and one component ($\varepsilon_z = \varepsilon_{||} < 0$) is negative. Figure 6 shows the frequency versus wave vector plot of $\log_{10} T$ for the evanescent waves for linear wave propagation. The appearance of transmission modes for low and high k values is obvious in Fig. 6. These transmitting bands are separated from each other by nontransmitting regions. Again we focus on the nonlinear wave propagation. Figures 7(a)–7(c) are density plots of $\log_{10} T$ at a constant frequency ($w = 1.2$) in the wave vector (k) versus intensity (I) planes. Different regions of Fig. 7(a) are magnified in Fig. 7(b) and 7(c); an emergence of patterns within patterns and fine separation of modes is again obvious in Fig. 7. The appearance of unstable fixed points (saddle) and divergence of stable trajectories in a hyperbolic manner is pictured in Fig. 7(b). Figure 7(c) shows the fine separation of high-k modes.

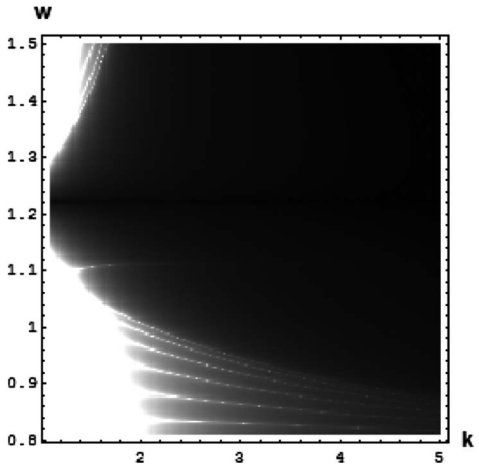

Fig. 6. Global transmission diagram of a Type I HMM.

Figures 8(a)–8(c) are density plots of $\log_{10} T$ in the wave vector versus intensity planes at a constant wave vector ($k = 3$). The same phenomenon of the appearance of self-similar fractal-like structures and fine separation of transmitting modes is also observed in Fig. 8.

The appearance of nonlinear high-k modes in both Type I and Type II HMMs is manifested with the help of diagrams. The presence of different periodic orbits and trajectories indicate the transmitting regions of these evanescent waves. Two types of behaviors are observed in both Type I and Type II HMMs. The appearance of saddle-like unstable fixed points and stable white transmitting trajectories are seen in the wave vector versus

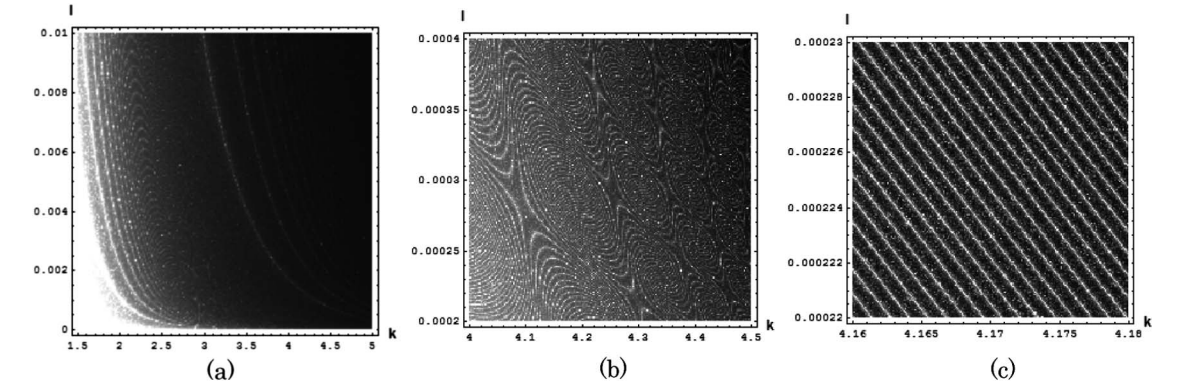

Fig. 7. (a) Plot of I versus k at $w = 1.2$ for a Type II HMM; (b) and (c) magnification of different portions of (a).

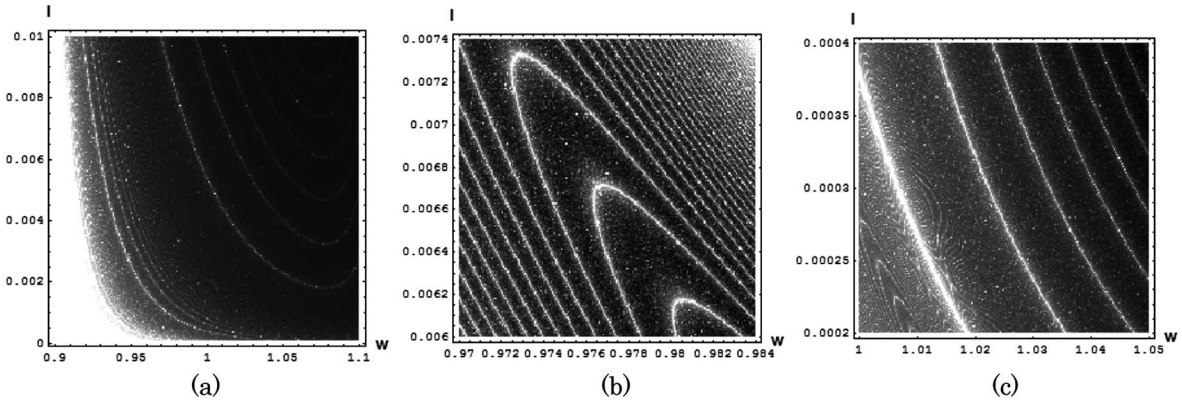

Fig. 8. (a) Plot of I versus w at $k = 3$ for a Type II HMM; (b) and (c) magnification of different portions of (a).

intensity plots at a fixed frequency. The frequency versus intensity plots at a given wave vector show the appearance of neutral central (elliptic) fixed points and white transmitting orbits around them. The magnification of these diagrams shows fine separation of these modes on the frequency versus intensity scale for a given wave vector and wave vector versus intensity scale for a given frequency. It is suggested that the properties of these nonlinear high-k modes can be further explored by explicitly deriving the equations of different periodic orbits and trajectories. The dependence on certain parameters such as the filling factor of the structure can also be investigated in another study.

References

1. M. Kauranen and A. V. Zayats, Nat. Photon. **6**, 737 (2012).
2. A. V. Zayats, I. I. Smolyaninov, and A. A. Maradudin, Phys. Rep. **408**, 13 (2005).
3. S. I. Maslovski, Opt. Commun. **285**, 3363 (2012).
4. R. Grimberg, A. Savin, and R. Steigmann, NDT & E Int. **46**, 70 (2012).
5. Y. Ben-Aryeh, Appl. Phys. B **91**, 157 (2008).
6. M. Memarian and G. V. Eleftheriades, IEEE Trans. Microw. Theory Technol. **60**, 3893 (2012).
7. O. Malyuskin and V. Fusco, IEEE Trans. Antennas Propag. **58**, 459 (2010).
8. P. A. Belov and Y. Hao, Phys. Rev. B **73**, 113110 (2006).
9. M. Lapine, I. V. Shadrivov, D. A. Powell, and Y. S. Kivshar, Nat. Mater. **11**, 30 (2011).
10. V. G. Veselago, Sov. Phys. Usp. **10**, 509 (1968).
11. J. P. Pendry, D. Schuring, and D. R. Smith, Science **312**, 1780 (2006).
12. W. Cai and V. Halaev, *Optical Metamaterials:Fundamentals and Applications* (Springer, 2009).
13. D. R. Smith, J. B. Pendry, and M. C. K. Wiltshire, Science **305**, 788 (2004).
14. R. A. Shelby, D. R. Smith, and S. Schultz, Science **292**, 77 (2001).
15. M. Zhong, Chin. Opt. Lett. **12**, 041601 (2014).
16. Y. Feng and Y. Liu, Chin. Opt. Lett. **13**, S12401 (2015).
17. V. P. Drachev, V. A. Podolskiy, and A. V. Kildishev, Opt. Express **21**, 15048 (2013).
18. A. Poddubny, I. Iorsh, P. Belov, and Y. Kivshar, Nat. Photon. **7**, 948 (2013).
19. C. L. Cortes, W. Newman, S. Molesky, and Z. Jacob, J. Opt. **14**, 063001 (2012).
20. C. Guclu, S. Campione, and F. Capolino, Phys. Rev. B **86**, 205130 (2012).
21. S. A. Biehs, M. Tschikin, and P. Ben–Abdallah, Phys. Rev. Lett. **109**, 104301 (2012).
22. Y. Chen, Y. Fang, S. Huang, X. Yan, and J. Shi, Chin. Opt. Lett. **11**, 061602 (2013).
23. P. Shekhar, J. Atkinson, and Z. Jacob, Nano Convergence **1**, 14 (2014).
24. A. N. Poddubny, P. A. Belov, and Y. S. Kivshar, Phys. Rev. A **84**, 023807 (2011).
25. G. V. Naik, J. Kim, and A. Boltasseva, Opt. Mater. Express **1**, 1090 (2011).
26. D. Lu and Z. Liu, Nat. Commun. **3**, 1205 (2012).
27. J. Kanungo and J. Schilling, Appl. Phys. Lett. **97**, 021903 (2010).
28. W. Dickson, G. Wurtz, P. Evans, D. O'Connor, R. Atkinson, R. Pollard, and A. V. Zayats, Phys. Rev. B **76**, 115411 (2007).
29. J. Schilling, Phys. Rev. E **74**, 046618 (2006).
30. P. A. Belov, Y. Zhao, S. Tse, P. Ikonen, M. G. Silveirinha, C. R. Simovski, S. Tretyakov, Y. Hao, and C. Parini, Phys. Rev. B **77**, 193108 (2008).
31. C. Lv, W. Li, X. Jiang, and J. Cao, Europhys. Lett. **105**, 28003 (2014).
32. S. V. Zhukovsky, O. Kidwai, and J. E. Sipe, Opt. Express **21**, 14982 (2013).
33. C. Argyropoulos, N. M. Estakhri, F. Monticone, and A. Alu, Opt. Express **21**, 15037 (2013).
34. C. Argyropoulos, F. Monticone, N. M. Estakhri, and A. Alu, Int. J. Antennas Propag. **2014**, 532634 (2014).
35. W. Li, Z. Liu, X. Zhang, and X. Jiang, Appl. Phys. Lett. **100**, 161108 (2012).
36. A. Madani, S. Zhong, H. Tajalli, S. R. Entezar, A. Namdar, and Y. Ma, Prog. Electromagn. Res. **143**, 545 (2013).
37. G. A. Wurtz, R. Pollard, W. Hendren, G. P. Wiederrecht, D. J. Gosztola, V. A. Podolskiy, and A. V. Zayats, Nat. Nanotechnol. **6**, 107 (2011).
38. G. Neira, G. Wurtz, P. Ginzburg, and A. Zayatz, Opt. Express **22**, 10987 (2014).
39. A. P. Slobozhanyuk, P. V. Kapitanova, D. S. Filonov, D. A. Powell, I. V. Shadrivov, M. Lapine, P. A. Belov, R. C. McPhedran, and Yu. S. Kivshar, Appl. Phys. Lett. **104**, 014104 (2014).
40. M. Lapine, I. V. Shadrivov, and Y. S. Kivshar, Rev. Mod. Phys. **86**, 1093 (2014).
41. C. Duncan, L. Perret, S. Palomba, M. Lapine, B. T. Kuhlmey, and C. M. de Sterke, Sci. Rep. **5**, 8983 (2015).
42. E. Lidorikis, Q. Li, and C. M. Soukoulis, Phys. Rev. B **54**, 10249 (1996).
43. Q. Li, C. T. Chan, K. M. Ho, and C. M. Soukoulis, Phys. Rev. B **53**, 15577 (1996).
44. C. C. Katsidis and D. I. Siapkas, App. Opt. **41**, 3978 (2002).
45. J. Li, Z. Li, and D. Zhang, Phys. Rev. E **75**, 056606 (2007).